Geophysical Research Letters

RESEARCH LETTER
10.1029/2025GL118489

Special Collection:
Exploring Carbon Cycling in Aquatic Ecosystems Using Novel Analytical and Data-Driven Approaches

Physical and Ecological Forcings Drive the Particle Dynamics and Enhanced Carbon Export Efficiency in the Tropical Marginal Sea

Zengchao Xu[1,2], Yibin Huang[1,3], Feipeng Xu[1], Yichong Wang[1,2], Wenxin Fan[1,2], Weinan Li[1,2], Jixin Chen[1], Xin Liu[1,2], and Bangqin Huang[1,2]

[1]State Key Laboratory of Marine Environmental Science, Xiamen University, Xiamen, China, [2]College of the Environment and Ecology, Xiamen University, Xiamen, China, [3]College of Ocean and Earth Sciences, Xiamen University, Xiamen, China

Abstract Marginal seas contribute disproportionately to the ocean carbon cycle but remain poorly constrained due to strong spatial and seasonal variability. Here, we combine newly collected in situ particle imagery with machine learning to reconstruct monthly, depth-resolved climatologies of particle biovolume and size distribution in the South China Sea, the largest tropical marginal sea in the North Pacific. Particle biovolume peaks in winter due to monsoon-driven mixing, with secondary summer maxima in regions influenced by upwelling and river plumes. Although particle size generally covaries with biovolume, seasonal decoupling occurs in plume-dominated zones. Applying a regionally optimized size-based model, we estimate an annual carbon export of 111.7 ± 6.0 Tg C yr^{-1}, corresponding to a high export efficiency of 17.5 ± 0.9%, exceeding typical low-latitude values. Our study integrates observational-modeling approaches to highlight the diverse physical and biogeochemical drivers of particle heterogeneity and an elevated biological pump efficiency in complex marginal sea.

Plain Language Summary Marginal seas, like the South China Sea, are small in area but play a big role in helping the ocean absorb, export and sequester carbon. However, we still don't fully understand how particles that carry carbon behave in these regions. In this study, we used new underwater camera observations combined with machine learning to track changes in particle amount and size throughout the year. We find clear seasonal patterns linked to winds, upwelling currents, and river input. Using these results, we estimate how much carbon sinks out of the surface ocean each year—about 111.7 million tons, with a relatively high efficiency compared to other warm ocean regions. Our findings show how local ocean conditions strongly affect carbon export, and highlight the value of combining new technologies with data modeling to study carbon movement in environmentally complex ocean region.

Key Points:

- Monthly particle characteristics in the South China Sea are reconstructed using optical imaging and machine learning
- Seasonal particle and size–volume relationships vary by regions, shaped by diverse physical and biogeochemical forcings
- A regional optimized model estimates carbon export of 111.7 ± 6.0 Tg C yr^{-1} with 17.5 ± 0.9% export efficiency

Supporting Information:

Supporting Information may be found in the online version of this article.

Correspondence to:

Y. Huang,
yibin.huang@xmu.edu.cn

Citation:

Xu, Z., Huang, Y., Xu, F., Wang, Y., Fan, W., Li, W., et al. (2026). Physical and ecological forcings drive the particle dynamics and enhanced carbon export efficiency in the tropical marginal sea. *Geophysical Research Letters*, *53*, e2025GL118489. https://doi.org/10.1029/2025GL118489

Received 30 JUL 2025
Accepted 19 MAR 2026

Author Contributions:

Conceptualization: Zengchao Xu, Yibin Huang, Bangqin Huang
Data curation: Zengchao Xu, Feipeng Xu
Funding acquisition: Yibin Huang, Xin Liu, Bangqin Huang
Investigation: Zengchao Xu, Feipeng Xu, Wenxin Fan
Methodology: Zengchao Xu, Yibin Huang, Weinan Li

1. Introduction

Marginal seas account for only 7%–8% of the global ocean area, yet they contribute ~28% of marine primary production and up to 80% of organic carbon burial (Dai et al., 2022; Keil, 2017). This disproportionate role makes them critical components of Earth's carbon cycle and climate system. As zones of intense ocean–land–atmosphere interaction and human activity, these regions are shaped by highly variable physical and biogeochemical processes (Song et al., 2025). Despite their importance, substantial uncertainties remain in our understanding of marginal sea ecosystem characteristics, carbon fluxes, and the mechanisms driving their spatiotemporal variability.

Particles play a central role in marine ecosystems and the biological carbon pump, serving as both indicators of ecological structure and the primary vectors of vertical carbon export (Boyd et al., 2019; Huang et al., 2023). Most particles originate from phytoplankton-derived particulate organic carbon (POC) and are continuously modified by biological processes (e.g., grazing, fragmentation, and remineralization) and physical–chemical interactions (e.g., aggregation, scavenging, and dissolution) (Cavan et al., 2021; Kwon et al., 2009; Shen et al., 2020). These transformations shape particle size and composition, which critically influence sinking velocities and, in turn, determine the efficiency of POC transfer to the deep ocean (Turner, 2015).

Traditional approaches for studying particle characteristics, such as bottle sampling, in situ pumps, and sediment traps, are labor-intensive and often limited in spatial and temporal resolution (Giering et al., 2020; Roca-Martí &

Supervision: Yibin Huang, Xin Liu, Bangqin Huang
Visualization: Zengchao Xu, Yichong Wang, Weinan Li, Jixin Chen
Writing – original draft: Zengchao Xu
Writing – review & editing: Zengchao Xu, Yibin Huang, Feipeng Xu, Yichong Wang, Wenxin Fan, Weinan Li, Jixin Chen, Xin Liu, Bangqin Huang

Puigcorbé, 2024). Although satellite remote sensing enables large-scale assessments of particle concentration and size structure (Balch & Mitchell, 2023; Kostadinov et al., 2009), it is restricted to the ocean surface. In recent years, non-invasive in situ imaging systems, particularly the Underwater Vision Profiler (UVP), have provided new opportunities to observe large particles (>100 μm) at high vertical and temporal resolution (Picheral et al., 2010). The UVP captures images in a defined volume (~1 L) and allows for automated estimation of particle abundance in a given size range (Picheral et al., 2010). UVP has been increasingly used to examine particle aggregation/disaggregation, zooplankton interactions, and vertical carbon fluxes (Guidi et al., 2015; Kiko et al., 2017; Liu et al., 2024; Xu, Zheng, et al., 2025). Notably, Kiko et al. (2022) compile a global UVP data set, and Clements et al. (2022, 2023) apply machine learning to model particle distributions and estimate export fluxes across diverse ecosystems. However, the scarcity of observations from low-latitude marginal seas in their data set limits the model's reliability in these dynamic environments (see Section 3.1).

In this study, we deploy the UVP5 optical imaging system during multiple cruises in the South China Sea (SCS)—a physically dynamic and ecologically complex marginal sea shaped by seasonal monsoons, river plumes, eddies, and Kuroshio intrusion (Ngo & Hsin, 2021; Tong et al., 2023; Wang et al., 2009; Xue et al., 2004). These new in situ observations enable direct, depth-resolved characterization of particle biovolume (BV) and size spectra. To upscale these measurements across space and time, we apply a machine learning approach that integrates satellite and reanalysis data, reconstructing monthly climatologies of particle characteristics. We then estimate POC export and export efficiency using a regionally optimized, size-based model. This integrated approach offers new constraints on the biological carbon pump in low-latitude marginal seas and demonstrates how the fusion of high-resolution observations and data-driven modeling can resolve particle dynamics and carbon fluxes in environmentally heterogeneous systems.

2. Methods

2.1. Particle Characteristics From UVP5 Observations

Particle profiles are collected using an optical imaging system (UVP5, Hydroptics, France) mounted on the CTD rosette during four cruises in the SCS: KK1904 (summer), KK2001 (spring), KK2205-1 (autumn), and KK2205-2 (winter), spanning 67 stations and 240 casts (Figure 1a; Figure S5 in Supporting Information S1). The UVP5 (mixed mode) captures images during the downcast at 20 frames s^{-1} with a descent rate of ~1 m s^{-1}. Following Picheral et al. (2010), particle images are binned into six size classes (100–125, 125–250, 250–500, 500–1,000, 1,000–2,000, and 2,000–5,000 μm), and data are averaged over 10 m depth intervals to improve large particle detection. Biovolume (BV, mm^3 m^{-3}) is calculated by summing the volume of all particles in a size class assuming spherical geometry (Equation 1):

$$\mathrm{BV} = \int_{s_{\min}}^{s_{\max}} \frac{\pi}{6} \times n(s) \times s^3 \tag{1}$$

where s is particle diameter (mm), and $n(s)$ is particle abundance in each bin. The particle size distribution (PSD) is described using a power-law relationship (Equation 2):

$$n(s) = n_0 \times s^{-\beta} \tag{2}$$

where $n(s)$ represents the abundance of particles within a given size range, and β denotes the PSD slope (Buonassissi & Dierssen, 2010). It is derived by performing a linear regression on the log-transformed, normalized particle abundance across size classes. A higher β indicates a greater proportion of smaller particles. The intercept n_0 is a size-independent coefficient corresponding to the regression's y-intercept. Only fits with $R^2 > 0.9$ are retained for further analysis. Profiles influenced by benthic resuspension are excluded based on visual identification of anomalously high large-particle concentrations near the bottom at 5 nearshore continental shelf stations (<100 m). In total, 18 profiles were removed during model construction (Figure S1 in Supporting Information S1). Sensitivity analyses show that if these resuspension-influenced profiles are included in the model, they lead to a substantial overestimation of carbon export at the base of the euphotic zone (Text S1, Figure S2 in Supporting Information S1). A total of 222 profiles from 62 stations are retained for subsequent analysis.

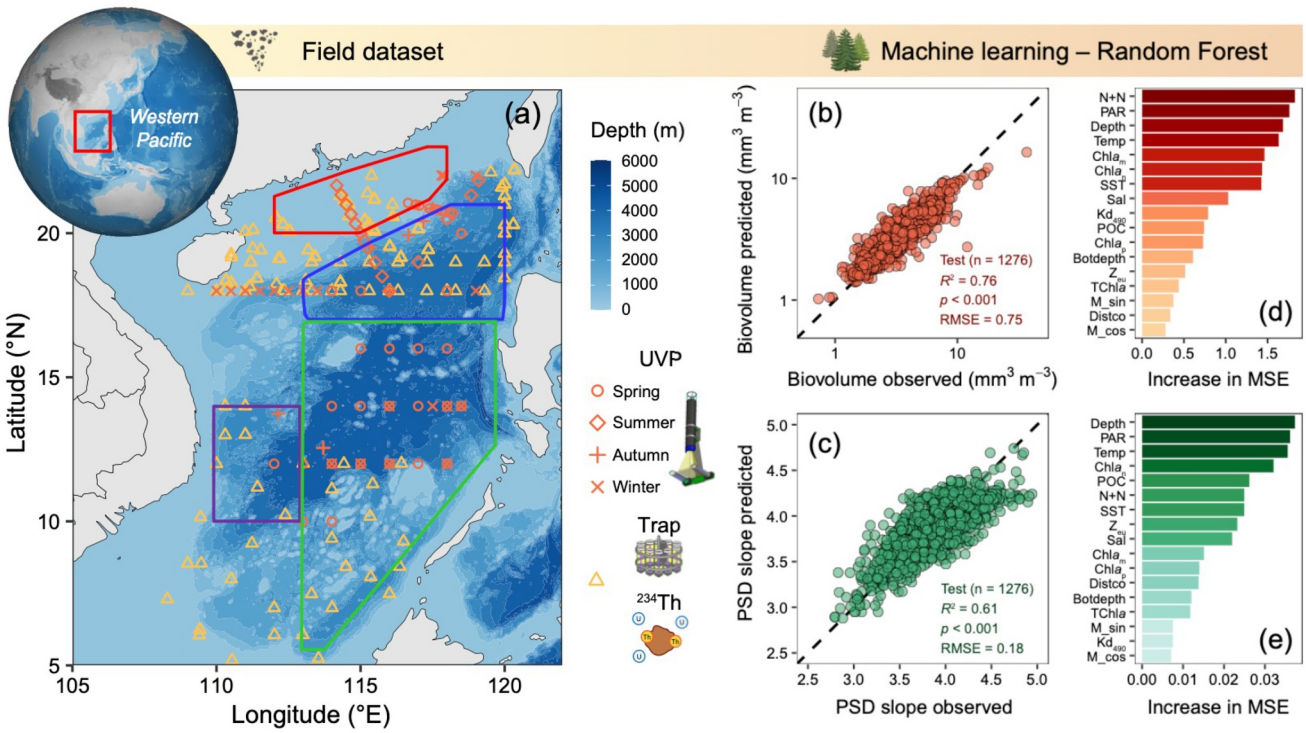

Figure 1. Sampling locations and Random Forest model performance for reconstructing particle characteristics in the South China Sea (SCS). (a) Locations of UVP5 sampling stations (orange) from four cruises covering four seasons. Yellow triangles represent historical particle organic carbon flux measurements from sediment traps or ^{234}Th–^{238}U disequilibrium used for regional model optimization. Four subregions of the SCS are outlined following Li et al. (2020), Shen et al. (2020), and Du et al. (2021): the Pearl River plume region (red), northern basin (blue), southern basin (green), and Vietnam upwelling region (purple). Background shading denotes water depth. (b, c) Model performance for biovolume (BV) and particle size distribution (PSD) slope using the validation data set. Dashed lines indicate 1:1 agreement. Note that higher PSD slopes indicate a greater proportion of small particles. (d, e) Ranked importance of environmental predictors in the Random Forest model, shown as the increase in mean squared error when each variable is permuted.

2.2. Upscaling UVP Observations Using a Machine Learning Approach

To extend the limited in situ UVP5 observations and better capture the spatial and temporal dynamics of particle characteristics at high spatiotemporal resolution, we employ a machine learning approach to reconstruct monthly climatologies of particle BV and PSD slope. Seventeen environmental predictors known to influence particle production and distribution are selected (Table S1, Texts S2, and S3 in Supporting Information S1), including sampling month, depth, bottom depth, offshore distance, euphotic depth, surface size-fractionated chlorophyll, surface light availability, depth-resolved temperature, depth-resolved salinity, and nutrient concentration. Sampling months are transformed using sine and cosine functions to account for their circular nature.

Environmental predictors are matched to UVP profiles by time, location, and depth. We use 70% of the data set for model training (n = 2,986) and withheld 30% for independent validation (n = 1,276). Random Forest models (implemented via the "*randomForest*" package in *R*) are separately constructed to predict particle BV and PSD slope from environmental variables. Details of hyperparameter tuning, selection, and model limitations are provided in Text S4 of Supporting Information S1.

2.3. POC Export Estimate Using a Locally Optimized Particle Size-Based Model

Following the framework of Guidi et al. (2008), the POC export flux (F_{POC}) can be expressed as the integral of the product of three particle size-dependent components (Equation 3): particle abundance $n(s)$, sinking velocity $w(s)$, and organic carbon content $c(s)$:

$$F_{\mathrm{POC}} = \int_{s_{\min}}^{s_{\max}} n(s) \times w(s) \times c(s)\, ds = \int_{s_{\min}}^{s_{\max}} \underbrace{n_0 \times s^{-\beta}}_{n(s)} \times \underbrace{m_0 \times s^{\mu}}_{w(s)\times c(s)}\, ds \tag{3}$$

Here, both sinking velocity and carbon content are approximated as power-law functions of particle size, such that $w(s) \cdot c(s) = m_0\, s^{\mu}$. Particle size distribution $n(s)$ follows a power-law distribution with exponent β, and n_0 is the intercept. The n_0 is derived from the observed BV and PSD slope (β) as (Equation 4):

$$n_0 = \frac{6 \times \mathrm{BV}}{\pi} \times \left(\frac{s_{\max}^{4-\beta}}{4-\beta} - \frac{s_{\min}^{4-\beta}}{4-\beta} \right)^{-1} \tag{4}$$

Upper and lower bounds of particle size ($s_{\min}$, $s_{\max}$) are set to 35 μm and 5 mm, respectively, consistent with the global UVP-based export framework by Clements et al. (2023).

To optimize m_0 and μ locally, we match in situ UVP profiles with historical ^{234}Th and sediment trap-based POC fluxes in the SCS (55 matched samples, Figure 1a; Text S2 in Supporting Information S1), using seasonal temporal windows (Spring: March–May; Summer: June–August; Autumn: September–November; and Winter: December–February) and 1° × 1° spatial bins, with UVP observations assigned to the closest available flux depth (depth difference ≤10 m). We then apply a Monte Carlo approach to determine the optimal set of coefficients, yielding $m_0 = 18.2 \pm 0.81$ and $\mu = 3.07 \pm 0.01$, which are broadly consistent with the global estimates ($m_0 = 18.0 \pm 2.8$, $\mu = 2.63 \pm 0.06$) reported by Clements et al. (2023). We acknowledge that this relatively coarse spatiotemporal pairing may overlook sub-seasonal variability and mesoscale physical influences. However, applying stricter matching criteria would drastically reduce the sample size and introduce greater uncertainty in Monte Carlo optimization due to data scarcity. A comparison between POC fluxes estimated using the global coefficients and our regionally optimized coefficients confirms that local optimization improves model accuracy in marginal seas (Figure S3 in Supporting Information S1). Looking forward, further refinement of particle-based export models could benefit from co-deployments of next-generation optical instruments such as the compact UVP6 and transmissometers (acting as optical sediment traps) on autonomous platforms (e.g., BGC-Argo floats and gliders) (Accardo et al., 2025; Picheral et al., 2022). This combination would enable high-resolution, synchronous measurements of particle characteristics and POC flux, thereby reducing spatiotemporal mismatches and improving model optimization.

2.4. Uncertainty Estimates

To quantify uncertainty in POC flux estimates, we consider contributions from model-derived uncertainty (σ_m) associated with the machine learning reconstruction of BV and PSD slope, parameter uncertainty in the locally optimized size-based export model (σ_p), as well as spatial (σ_s) and temporal variability (σ_t) across grids and months. We use a Monte Carlo framework with 1,000 iterations, in which we randomly reassemble the training data set in the Random Forest to account for σ_m, while simultaneously perturbing the export model coefficients m_0 and μ by sampling from normal distributions based on their fitted uncertainties (0.81 and 0.01, respectively, See Section 2.3). All uncertainty sources are propagated to POC flux estimates, and the total uncertainty is calculated as the root-sum-square of all components: $\sqrt{\sigma_m^2 + \sigma_p^2 + \sigma_s^2 + \sigma_t^2}$.

3. Results and Discussion

3.1. Data-Driven Model for Particle Characteristics Reconstruction

We conduct the high-resolution, vertical observations of particle characteristics in a low-latitude marginal sea using UVP5 deployment during various cruises spanning four seasons (Figure 1a), thereby helping to fill a critical observational gap in low-latitude marginal seas (Kiko et al., 2022). Observed particle BV, averaged over the euphotic zone across multiple cruises and stations, varies from 1.47 to 31.05 mm^3 m^{-3}, showing a pronounced coastal-to-offshore decline (Figure S4a in Supporting Information S1). Mean PSD slopes ranged from 3.27 to 4.60, with higher values offshore, indicating a greater fraction of small particles (Figure S4b in Supporting Information S1). We compare our field observations with the projection from the global UVP-based machine learning model developed by Clements et al. (2022) and find that it substantially underestimates BV in the SCS

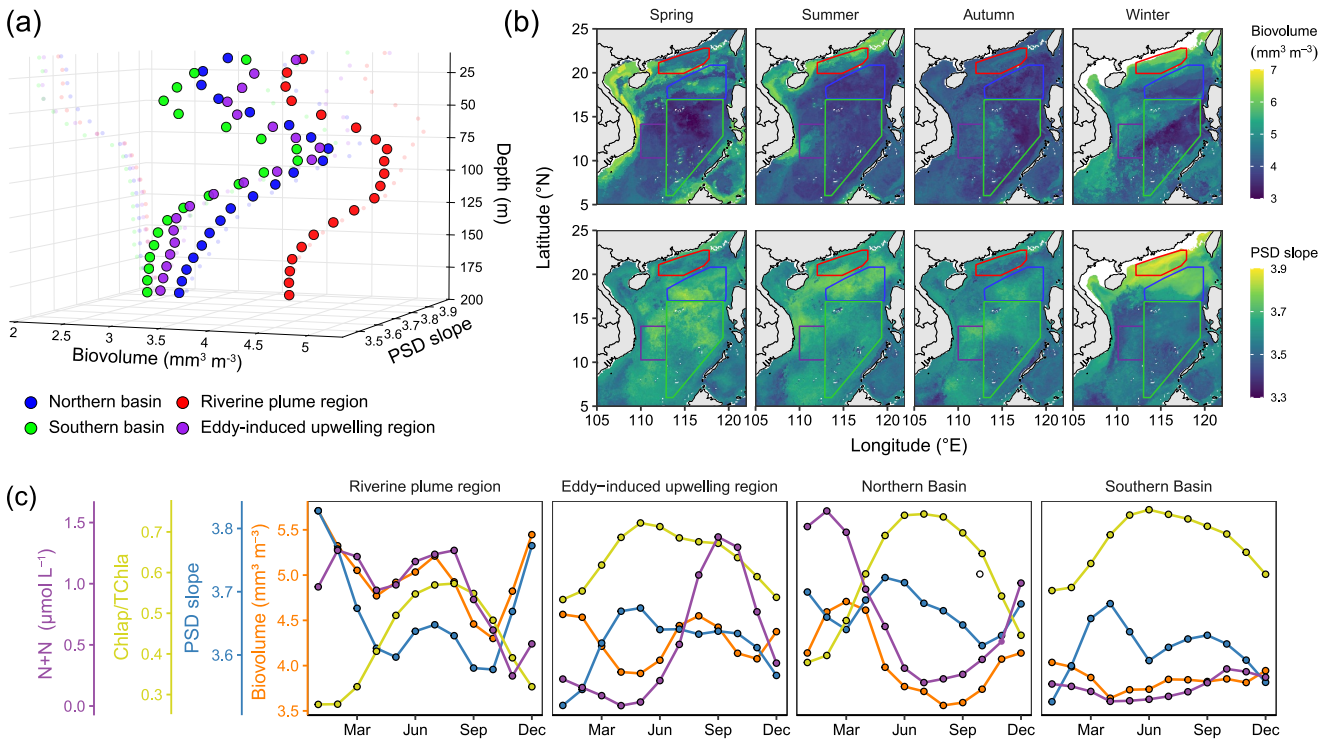

Figure 2. Seasonal and spatial variability in particle biovolume (BV) and particle size distribution (PSD) slope reconstructed via a machine learning approach in the South China Sea (SCS). (a) Depth-resolved mean profiles of BV and PSD slope in four sub-regions: Pearl River plume region (red), Vietnam eddy-induced upwelling region (purple), northern basin (blue), and southern basin (green). The mean value in the Pearl River plume region is calculated only for deep waters (>200 m) to avoid signals introduced by bottom resuspension. The 2-D version is provided in Figure S10 of Supporting Information S1. (b) Seasonal maps of euphotic-zone averaged BV (top) and PSD slope (bottom). A higher PSD slope value indicates a greater proportion of smaller particles. Spring: March–May; Summer: June–August; Autumn: September–November; and Winter: December–February. (c) Monthly climatologies of euphotic-zone BV, PSD slope, nitrate and nitrite concentration (N + N), and the fractional contribution of pico-phytoplankton to total chlorophyll-*a* ($Chla_p$/TChl*a*) in each sub-region. Panel (c) with error bars is presented in Figure S11 of Supporting Information S1.

(predicted range: 0.46–1.33 mm^3 m^{-3}). Moreover, it failed to reproduce the spatial variability in PSD (predicted range: 3.80–3.92; Figure S4 in Supporting Information S1). These discrepancies likely stem from the lack of low-latitude marginal-sea data in the training set and the model's coarse resolution (1° × 1°). Our results underscore the need for regionally trained, high-resolution models to accurately resolve particle dynamics in marginal seas.

Vertically, particle BV exhibits a pronounced subsurface maximum (~80 m) (Figure 2a), closely aligned with the deep chlorophyll maximum (DCM, ~80 m) detected by CTD-mounted fluorescence sensors (Figure S6 in Supporting Information S1). A similar pattern has been reported by Trudnowska et al. (2021), who documented elevated zooplankton abundance near ~40 m and enhanced particle concentrations near ~75 m, corresponding to depths adjacent to DCM. Their particle morphology analyses suggest that these subsurface maxima are predominantly of biogenic origin, reflecting multiple contributing processes, including relatively high phytoplankton biomass (despite increased Chl:C ratios associated with photoacclimation [Marañón et al., 2021]) and the accumulation of sinking phytoplankton aggregates and zooplankton fecal pellets (Trudnowska et al., 2021). Collectively, these mechanisms can elevate particle concentrations in the vicinity of the DCM and may help explain the comparatively high carbon export potential observed at this depth. Particle size generally decreases with depth (Figure 2a). In subsurface layers, where light becomes limiting (Dai et al., 2023), the ecosystem shifts from net autotrophy to net heterotrophy. As particles sink, they are subject to microbial degradation and zooplankton-mediated fragmentation, leading to an increasing proportion of smaller particles with depth (Bressac et al., 2024; Cram et al., 2022).

We apply a machine learning algorithm to model the relationship between particle characteristics and environmental variables. The model performs well on independent validation data, with strong agreement between predicted and observed values ($R^2 = 0.76$, $p < 0.001$, RMSE = 0.75 mm^3 m^{-3} for BV; $R^2 = 0.61$, $p < 0.001$, and

RMSE = 0.18 for PSD slope; Figures 1b and 1c). Variable importance analysis reveal that nutrient, PAR, and depth are the most important predictors for particle BV, while PSD slope is primarily influenced by PAR, depth, and temperature (Figures 1d and 1e), consistent with their established roles in regulating phytoplankton production and community structure (Cullen, 2015; Mignot et al., 2014; Xiao et al., 2018).

3.2. Distinct Physicochemical Forcings Shape Sub-Regional Particle Dynamics

We apply the trained machine learning model to gridded environmental data sets to generate monthly climatologies of depth-resolved BV and PSD slope across the SCS at a high spatial resolution (0.083°; Figure 2; Figures S7 and S8 in Supporting Information S1). This approach enables a comprehensive view of particle field variability and offers a basis for understanding how regional hydrographic and biogeochemical gradients influence particle characteristics. To facilitate comparisons, we divide the SCS into four ecologically distinct sub-regions based on particle patterns and previous regional classifications (Du et al., 2021; Li et al., 2020; Shen et al., 2020): (a) the River plume region influenced by Pearl riverine input, (b) the eddy-induced upwelling region off Vietnam, (c) the oligotrophic northern basin with strong winter mixing, and (d) the oligotrophic southern basin with a relatively stable stratification over the course of year (Figure 1a).

Overall, particle BV in the euphotic zone is highest in the Riverine plume region, followed by the eddy-induced upwelling region and the northern basin, and lowest in the southern basin (Figures 2a and 2b). This spatiotemporal pattern is consistent with regional gradients in nutrient concentrations (Figure 2c) and primary productivity (Du et al., 2021; Song et al., 2023; Xie et al., 2020). It is worth noting that nutrient is among the most important predictors in our BV model, with an independent test yielding an R^2 of 0.3 between nutrient and BV (Figure S9 in Supporting Information S1). Although net primary production (NPP) was not included explicitly as a predictor in our model, NPP is often highly correlated with light, nutrient availability, and biomass. Therefore, while the apparent explanatory power of nutrient and productivity gradients on BV is strong, these associations should be interpreted with caution, as they do not necessarily imply direct causation. Nonetheless, the observed covariation of these environmental factors aligns well with known spatiotemporal patterns of physical processes in different regions of the SCS, providing a plausible mechanistic basis for the relationships we inferred. In low-latitude marginal seas, where light and temperature are generally sufficient, nutrient availability is the primary factor controlling phytoplankton distribution (Dai et al., 2023). Nutrient-rich conditions in the plume and upwelling regions stimulate phytoplankton growth and support elevated particle concentrations (Chen, 2005; Hu et al., 2015; O'Connor et al., 2016). In contrast, the northern and southern basins are relatively oligotrophic due to effective isolation from land-derived inputs by the central gyre circulation (Dai et al., 2013; Hu et al., 2000). In general, nutrient-replete regions are dominated by large-celled phytoplankton groups such as diatoms and dinoflagellates (Xiao et al., 2018). These taxa actively secrete acidic polysaccharides that promote the formation of large particle aggregates, including transparent exopolymer particles (Huang et al., 2021; Passow, 2002; Vidal-Melgosa et al., 2021). In oligotrophic basins, the phytoplankton community is typically composed of small-celled taxa such as *Prochlorococcus*, *Haptophytes*, and *Synechococcus* (Xiao et al., 2018). Although these small cells contribute less directly to large-particle formation, zooplankton grazing and repackaging processes facilitate the transformation of small particles into larger fecal aggregates (Stukel et al., 2013; Turner, 2015). As a result, while particle size generally follows the same spatial trend as BV, its regional variability is less pronounced.

Seasonal variations in particle properties display distinct spatial patterns shaped by region-specific physical forcings. All four sub-regions exhibit a primary BV peak in winter or early spring (Riverine plume region: 5.7 ± 0.2, Eddy-induced upwelling region: 4.6 ± 0.6, Northern basin: 4.7 ± 1.8, Southern basin: 4.1 ± 0.7 $mm^3\ m^{-3}$) (orange line in Figure 2c), primarily driven by northeast monsoon–induced convective mixing that enhances nutrient supply and promotes phytoplankton growth (Tseng et al., 2005; Xie et al., 2020). In the northern basin near the Luzon Strait, this signal is further amplified by frontal activity associated with intensified Kuroshio intrusion (Li et al., 2025). In addition to phytoplankton growth, zooplankton grazing represents another potential mechanism contributing to BV peaks. Chen et al. (2013) conducted dilution experiments in the northern SCS and estimated that microzooplankton consumed approximately 60%–80% of daily primary production, with grazing intensity generally higher on the continental shelf and slope compared to the central basin. Furthermore, food-web models that incorporate zooplankton grazing better simulate carbon export in the SCS (Figure 3e) and underscore the key role of grazing in particle formation and export. Both field observations and food-web modeling consistently show that, relative to winter, the plume region in summer exhibits markedly higher grazing pressure, which can increase fecal pellet flux and is associated with a greater proportion of large

10.1029/2025GL118489

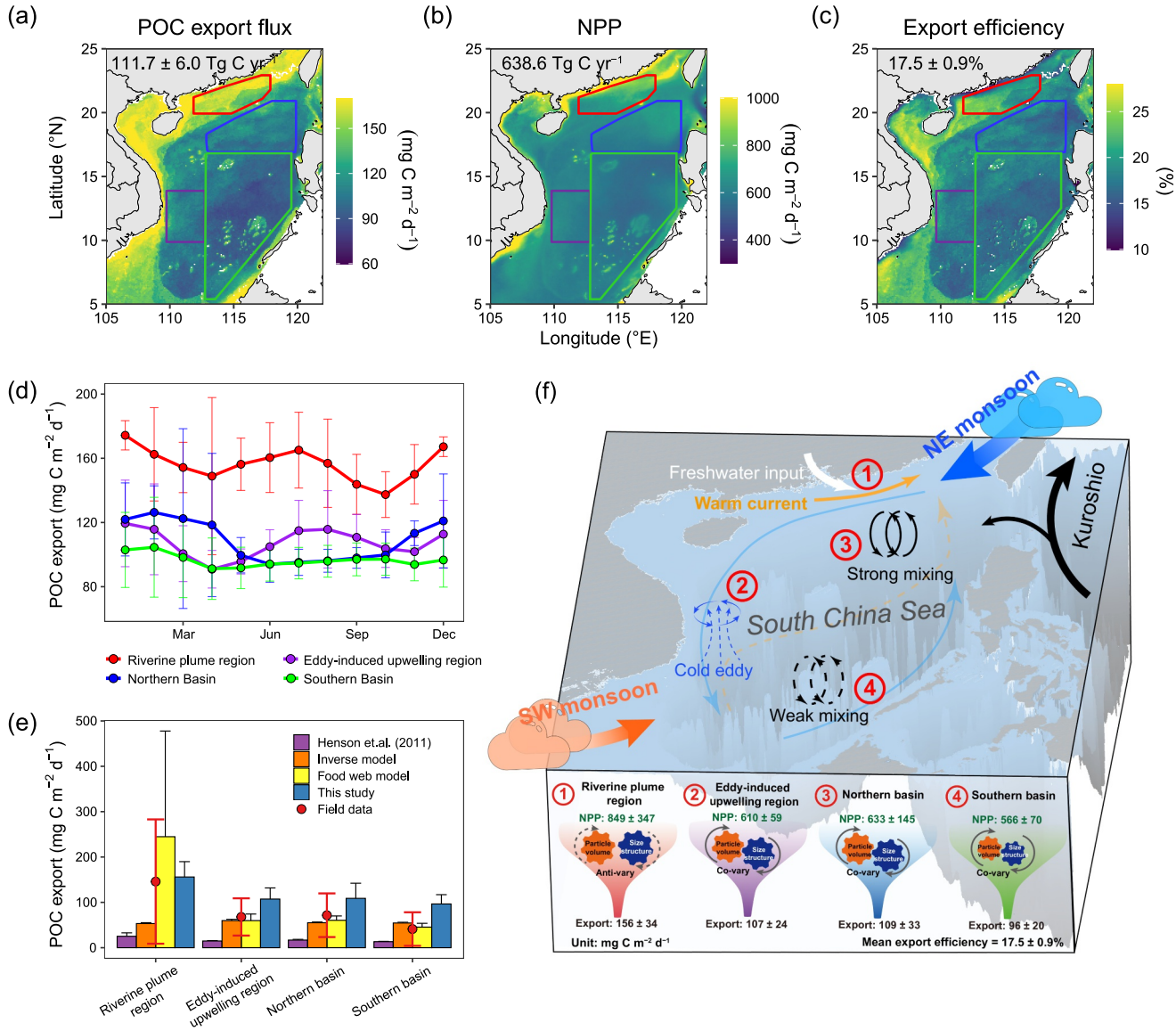

Figure 3. (a) Annual mean particulate organic carbon (POC) export flux at the base of the euphotic zone, estimated from reconstructed particle biovolume (BV) and particle size distribution (PSD) using a regionally optimized model. (b) Annual mean net primary production (NPP) derived from the absorption-based productivity model. (c) Export efficiency, calculated as the ratio of POC export to NPP. The area cumulative annual POC export, NPP, and export efficiency are indicated in the top left corner in panels a–c, respectively; error bars indicate ± propagated error. (d) Seasonal variation in POC export across four sub-regions. (e) Comparison of POC export estimates from this study and other models; error bars indicate ± propagated error. (f) Conceptual diagram illustrating how distinct physical processes drive regional differences in BV, PSD, and POC export across four sub-regions of the South China Sea (SCS).

particles, jointly enhancing export efficiency (Chen et al., 2013; Li et al., 2018). A secondary BV peak occurs in summer in both the Pearl River plume (5.2 ± 0.7 mm^3 m^{-3}) and Vietnam upwelling regions (4.6 ± 0.8 mm^3 m^{-3}), driven by contrasting mechanisms: nutrient-rich riverine discharge and eddy-induced upwelling, respectively (Ngo & Hsin, 2021; Tong et al., 2023).

In most sub-regions, seasonal variations of PSD generally vary inversely with BV (Spearman's $\rho = -0.64$, $p < 0.05$ in eddy-induced upwelling; $\rho = -0.62$, $p < 0.05$ in central basin) and align with satellite-derived chlorophyll size class distributions (yellow line in Figure 2c), reflecting a dominance of smaller cells in high PSD slope conditions. However, in the Pearl River plume during summer, both BV and PSD slope increase simultaneously ($\rho = 0.90$, $p < 0.001$), indicating a shift toward smaller-sized particles despite elevated particle abundance. This decoupling likely reflects local ecological shifts driven by nutrient imbalance and food web

interactions. Nitrogen-rich but silicon- and phosphorus-poor freshwater in Pearl River plume region can limit large diatoms and favor small phytoplankton, while grazing pressure may further reduce large cells and reinforce community downsizing (Chen et al., 2013; Tong et al., 2023). Similar phenomena have also been observed in the California Current and the Arabian Sea upwelling systems (Clements et al., 2022).

3.3. New Estimate in POC Flux by Locally Optimized Particle Size-Based Model

We estimate euphotic-zone POC export across the SCS by combining monthly climatologies of gridded BV and PSD slope with a locally optimized size-based model (see Section 2.3). Predicted annual average POC export fluxes average 156 ± 34 mg C m^{-2} d^{-1} in the riverine plume region, 107 ± 24 mg C m^{-2} d^{-1} in the eddy-induced upwelling region, 109 ± 33 mg C m^{-2} d^{-1} in the northern basin, and 96 ± 20 mg C m^{-2} d^{-1} in the southern basin (**blue bars in** Figure 3e), closely aligning with sediment trap and ^{234}Th-based observations (red dots in Figure 3e). Some of patchy high values in the southern basin are attributed to the islands and reefs (Figure S12 in Supporting Information S1). Further analysis reveals that export fluxes are strongly correlated with particle BV across sub-regions (Figure S13a in Supporting Information S1), and generally increase with particle size (Figure S13b in Supporting Information S1), suggesting that higher BV is typically associated with larger, faster-sinking particles. The Pearl River plume is an exception, where a weak negative correlation between export and particle size is observed (Figure S13b in Supporting Information S1). However, the slope is flat, indicating that particle size has only a minor offsetting effect on export in this region. Overall, BV emerges as the dominant predictor of POC export, with BV and POC flux exhibiting consistent spatial and seasonal patterns and elevated values over the shelf and slope (Figures 2b, 3a, and 3d; Figures S13a and S14 in Supporting Information S1).

Our estimate yields a basin-scale euphotic-zone POC export of 111.7 ± 6.0 Tg C yr^{-1} in the SCS (Figure 3a), providing a new constraint on biological pump strength in this dynamic marginal sea. This estimate is approximately 2.5 times higher than the carbon export by Clements et al. (2023) for our study region (Figure S15d in Supporting Information S1), which is derived using the same particle size-based approach but with gridded particle properties and coefficients trained on global data sets. The discrepancy underscores the potential underestimation of POC export in tropical marginal seas by global-scale models. Notably, our estimate aligns well with predictions from a locally optimized food-web model (112.5 Tg C yr^{-1}) (Figure S15b in Supporting Information S1), which captures the broad coastal-to-offshore gradient but lacks the resolution to distinguish finer spatial differences among sub-basins (e.g., northern vs. southern basins, Luzon Strait or localized upwelling zones) (Li et al., 2018). In contrast, the empirical model by Henson et al. (2011), which estimates POC export based on NPP and a temperature-dependent export efficiency, underestimates the flux by nearly an order of magnitude (16.2 Tg C yr^{-1}) (Figure S15a in Supporting Information S1), while a global inverse model trained on hydrographic profiles predicts an intermediate export (55.9 Tg C yr^{-1}) but fails to resolve spatial heterogeneity (Figure S15c in Supporting Information S1) (Nowicki et al., 2022).

Given satellite-derived NPP (based on absorption-based productivity model [AbPM]) of 638.6 Tg C yr^{-1}, our results suggest an average export efficiency of 17.5 ± 0.9% (Figures 3b, 3c, and 3f). We also compare the e-ratio estimated using NPP derived from three commonly used satellite-based models (VGPM, CbPM, and CAFE), which yielded values ranging from 17.0% to 26.2% (Figure S16 in Supporting Information S1). Overall, our conclusions are robust across different NPP models (Text S5 in Supporting Information S1), as the estimated e-ratios are consistently substantially higher than those reported for other low-latitude regions (e.g., ∼7% in subtropical gyres) and are comparable to values observed in subpolar systems (11%–25%) (Bacon et al., 1996; Buesseler & Boyd, 2009; Buesseler et al., 2007, 2008). This elevated export efficiency likely reflects enhanced nutrient supply driven by regional physical processes such as monsoon-driven mixing, eddy-induced upwelling, and riverine inputs aforementioned (Figure 3f). In the oligotrophic basin of SCS, previous studies have also identified a positive relationship between POC export and the relative abundance of haptophytes, a group of mixotrophic and partially calcifying phytoplankton (Cai et al., 2015). Their presence may enhance export through ballasting effects and more efficient trophic transfer (Tréguer et al., 2018). Together, these findings highlight the distinct physical and ecological controls that drive disproportionately high export in marginal seas.

The estimation of the e-ratio in this study is based on Eulerian framework, which implicitly assumes spatial coupling between primary production and carbon export. In strongly advective systems, such as the California Current Ecosystem, lateral transport driven by Ekman currents, filaments, and mesoscale eddies can lead to substantial spatial decoupling between production and export, with offsets of up to ∼300 km (Chabert et al., 2021;

Gruber et al., 2011). In our highly dynamic study region, evidence from BGC-Argo observations, sediment traps, and black-carbon constrained mass balance models indicates significant lateral inputs of POC associated with plume- and eddy-driven transport, turbidity flows, and subsurface circulation (Schroeder et al., 2015; Shen et al., 2020; Yang et al., 2021). Accordingly, the e-ratio should be interpreted as a regional, area-integrated diagnostic metric, rather than a strictly local measure of biological pump efficiency. Future progress will require Lagrangian observations combined with high-resolution coupled physical–biogeochemical models.

4. Conclusion

This study provides a spatially and temporally resolved assessment of particle characteristics and carbon export in a low-latitude marginal sea, based on in situ UVP5 observations and machine learning reconstructions. SCS shows pronounced regional and seasonal variability in particle BV and size structure, shaped by distinct physical drivers such as monsoon-induced mixing, riverine discharge, and eddy-driven upwelling. These processes generate characteristic particle regimes across ecological sub-regions. A regionally optimized size-spectrum model yields an annual carbon export of 111.7 ± 6.0 Tg C yr^{-1} and a relatively high export efficiency of 17.5 ± 0.9%, which exceeds typical values for subtropical gyres and equatorial oceans. We show that particle BV is the dominant control on POC export, while particle size exerts a secondary but regionally specific influence. Comparison with global models reveals their limited ability to resolve fine-scale heterogeneity in marginal seas. Overall, our findings highlight the outsized role of marginal seas in ocean carbon cycling and emphasize the need for high-resolution, observation-constrained models to capture the coupled physical-ecological processes that regulate particle dynamics and export in these dynamic systems.

Conflict of Interest

The authors declare no conflicts of interest relevant to this study.

Availability Statement

UVP5 data from field cruise and POC export flux at the base of the euphotic zone, estimated from reconstructed particle biovolume and size distribution using a regionally optimized model are available at Zenodo (Xu, Huang, et al., 2025). NASA Ocean Color products for SST, POC, Kd_{490}, TChl*a*, PAR, and Z_{eu} can be accessed at https://oceandata.sci.gsfc.nasa.gov/l3/. Vertical temperature and salinity profiles are available at Copernicus Marine reanalysis (European Union-Copernicus Marine Service, 2018). Phytoplankton size classes data used in the study are available at Liu et al. (2021). Nutrient data used in the study are available at Du et al. (2021). The distance to coast data is retrieved from the NASA Ocean Biology Processing Group ancillary resources (https://oceancolor.gsfc.nasa.gov/resources/docs/distfromcoast/). Historical POC flux observations used for model optimization are available at Cai et al. (2008), Cai et al. (2015), Ho et al. (2010), Hung and Gong (2010), Shih et al. (2019), Wei et al. (2011), and Zhou et al. (2013). Outputs from comparison models are available at Li et al. (2018), Nowicki et al. (2022), and Henson et al. (2011). The AbPM-derived NPP estimates are available at Song et al. (2023).

Acknowledgments

This study was supported by the National Natural Science Foundation of China (Grant 42130401, 42406099, 42122044, 42141002), and Natural Science Foundation of Fujian Province (Grant 2025J09005). Data and samples were collected onboard R/V Tan Kah Kee of Xiamen University implementing the open research cruises KK1904, NORC2019-06, NORC2022-06 supported by NSFC Shiptime Sharing Project (project number: 41849901, 41949901). We thank Prof. Rainer Kiko (GEOMAR Helmholtz Centre for Ocean Research Kiel) for his insightful comments and suggestions that helped improve the manuscript. We thank the team led by Prof. Zhongping Lee for developing the AbPM. We also thank Lizhen Lin, Yiyong Jiang and Yiwei Shang for their assistance in deploying UVP5. This study was also supported by Natural Science Foundation of Xiamen, China (Grant 3502Z202472006), and Fundamental Research Funds for the Central Universities (Grant 20720240105 and 20720240053).

References

Accardo, A., Laxenaire, R., Baudena, A., Speich, S., Kiko, R., & Stemmann, L. (2025). Intense and localized export of selected marine snow types at eddy edges in the South Atlantic Ocean. *Biogeosciences*, *22*(5), 1183–1201. https://doi.org/10.5194/bg-22-1183-2025

Bacon, M. P., Cochran, J. K., Hirschberg, D., Hammar, T. R., & Fleer, A. P. (1996). Export flux of carbon at the equator during the EqPac time-series cruises estimated from 234Th measurements. *Deep Sea Research Part II: Topical Studies in Oceanography*, *43*(4), 1133–1153. https://doi.org/10.1016/0967-0645(96)00016-1

Balch, W. M., & Mitchell, C. (2023). Remote sensing algorithms for particulate inorganic carbon (PIC) and the global cycle of PIC. *Earth-Science Reviews*, *239*, 104363. https://doi.org/10.1016/j.earscirev.2023.104363

Boyd, P. W., Claustre, H., Levy, M., Siegel, D. A., & Weber, T. (2019). Multi-faceted particle pumps drive carbon sequestration in the ocean. *Nature*, *568*(7752), 327–335. https://doi.org/10.1038/s41586-019-1098-2

Bressac, M., Laurenceau-Cornec, E. C., Kennedy, F., Santoro, A. E., Paul, N. L., Briggs, N., et al. (2024). Decoding drivers of carbon flux attenuation in the oceanic biological pump. *Nature*, *633*(8030), 1–7. https://doi.org/10.1038/s41586-024-07850-x

Buesseler, K. O., & Boyd, P. W. (2009). Shedding light on processes that control particle export and flux attenuation in the twilight zone of the open ocean. *Limnology & Oceanography*, *54*(4), 1210–1232. https://doi.org/10.4319/lo.2009.54.4.1210

Buesseler, K. O., Lamborg, C. H., Boyd, P. W., Lam, P. J., Trull, T. W., Bidigare, R. R., et al. (2007). Revisiting carbon flux through the ocean's twilight zone. *Science*, *316*(5824), 567–570. https://doi.org/10.1126/science.1137959

Buesseler, K. O., Trull, T. W., Steinberg, D. K., Silver, M. W., Siegel, D. A., Saitoh, S.-I., et al. (2008). VERTIGO (VERtical transport In the global ocean): A study of particle sources and flux attenuation in the North Pacific. *Deep Sea Research Part II: Topical Studies in Oceanography*, *55*(14), 1522–1539. https://doi.org/10.1016/j.dsr2.2008.04.024

Buonassissi, C. J., & Dierssen, H. M. (2010). A regional comparison of particle size distributions and the power law approximation in oceanic and estuarine surface waters. *Journal of Geophysical Research*, *115*(C10). https://doi.org/10.1029/2010JC006256

Cai, P., Chen, W., Dai, M., Wan, Z., Wang, D., Li, Q., et al. (2008). A high-resolution study of particle export in the southern South China Sea based on 234Th:238U disequilibrium. *Journal of Geophysical Research*, *113*(C4). https://doi.org/10.1029/2007JC004268

Cai, P., Zhao, D., Wang, L., Huang, B., & Dai, M. (2015). Role of particle stock and phytoplankton community structure in regulating particulate organic carbon export in a large marginal sea. *Journal of Geophysical Research: Oceans*, *120*(3), 2063–2095. https://doi.org/10.1002/2014JC010432

Cavan, E. L., Kawaguchi, S., & Boyd, P. W. (2021). Implications for the mesopelagic microbial gardening hypothesis as determined by experimental fragmentation of Antarctic krill fecal pellets. *Ecology and Evolution*, *11*(2), 1023–1036. https://doi.org/10.1002/ece3.7119

Chabert, P., d'Ovidio, F., Echevin, V., Stukel, M. R., & Ohman, M. D. (2021). Cross-shore flow and implications for carbon export in the California current ecosystem: A lagrangian analysis. *Journal of Geophysical Research: Oceans*, *126*(2), e2020JC016611. https://doi.org/10.1029/2020JC016611

Chen, B., Zheng, L., Huang, B., Song, S., & Liu, H. (2013). Seasonal and spatial comparisons of phytoplankton growth and mortality rates due to microzooplankton grazing in the northern South China Sea. *Biogeosciences*, *10*(4), 2775–2785. https://doi.org/10.5194/bg-10-2775-2013

Chen, Y.-L. L. (2005). Spatial and seasonal variations of nitrate-based new production and primary production in the South China Sea. *Deep Sea Research Part I: Oceanographic Research Papers*, *52*(2), 319–340. https://doi.org/10.1016/j.dsr.2004.11.001

Clements, D. J., Yang, S., Weber, T., McDonnell, A. M. P., Kiko, R., Stemmann, L., & Bianchi, D. (2022). Constraining the particle size distribution of large marine particles in the global ocean with in situ optical observations and supervised learning. *Global Biogeochemical Cycles*, *36*(5), e2021GB007276. https://doi.org/10.1029/2021GB007276

Clements, D. J., Yang, S., Weber, T., McDonnell, A. M. P., Kiko, R., Stemmann, L., & Bianchi, D. (2023). New estimate of organic carbon export from optical measurements reveals the role of particle size distribution and export horizon. *Global Biogeochemical Cycles*, *37*(3), e2022GB007633. https://doi.org/10.1029/2022GB007633

Cram, J. A., Fuchsman, C. A., Duffy, M. E., Pretty, J. L., Lekanoff, R. M., Neibauer, J. A., et al. (2022). Slow particle remineralization, rather than suppressed disaggregation, drives efficient flux transfer through the Eastern Tropical North Pacific oxygen deficient zone. *Global Biogeochemical Cycles*, *36*(1), e2021GB007080. https://doi.org/10.1029/2021GB007080

Cullen, J. J. (2015). Subsurface chlorophyll maximum layers: Enduring enigma or mystery solved? *Annual Review of Marine Science*, *7*(Volume 7, 2015), 207–239. https://doi.org/10.1146/annurev-marine-010213-135111

Dai, M., Cao, Z., Guo, X., Zhai, W., Liu, Z., Yin, Z., et al. (2013). Why are some marginal seas sources of atmospheric CO2? *Geophysical Research Letters*, *40*(10), 2154–2158. https://doi.org/10.1002/grl.50390

Dai, M., Luo, Y.-W., Achterberg, E. P., Browning, T. J., Cai, Y., Cao, Z., et al. (2023). Upper ocean biogeochemistry of the oligotrophic North Pacific Subtropical Gyre: From nutrient sources to carbon export. *Reviews of Geophysics*, *61*(3), e2022RG000800. https://doi.org/10.1029/2022RG000800

Dai, M., Su, J., Zhao, Y., Hofmann, E. E., Cao, Z., Cai, W.-J., et al. (2022). Carbon fluxes in the coastal ocean: Synthesis, boundary processes, and future trends. *Annual Review of Earth and Planetary Sciences*, *50*(1), 593–626. https://doi.org/10.1146/annurev-earth-032320-090746

Du, C., He, R., Liu, Z., Huang, T., Wang, L., Yuan, Z., et al. (2021). Climatology of nutrient distributions in the South China Sea based on a large data set derived from a new algorithm. *Progress in Oceanography*, *195*, 102586. https://doi.org/10.1016/j.pocean.2021.102586

European Union-Copernicus Marine Service. (2018). Global ocean physics reanalysis [Dataset]. *Mercator Ocean International*. https://doi.org/10.48670/MOI-00021

Giering, S. L. C., Cavan, E. L., Basedow, S. L., Briggs, N., Burd, A. B., Darroch, L. J., et al. (2020). Sinking organic particles in the ocean—flux estimates from in situ optical devices. *Frontiers in Marine Science*, *6*, 834. https://doi.org/10.3389/fmars.2019.00834

Gruber, N., Lachkar, Z., Frenzel, H., Marchesiello, P., Münnich, M., McWilliams, J. C., et al. (2011). Eddy-induced reduction of biological production in eastern boundary upwelling systems. *Nature Geoscience*, *4*(11), 787–792. https://doi.org/10.1038/ngeo1273

Guidi, L., Jackson, G. A., Stemmann, L., Miquel, J. C., Picheral, M., & Gorsky, G. (2008). Relationship between particle size distribution and flux in the mesopelagic zone. *Deep Sea Research Part I: Oceanographic Research Papers*, *55*(10), 1364–1374. https://doi.org/10.1016/j.dsr.2008.05.014

Guidi, L., Legendre, L., Reygondeau, G., Uitz, J., Stemmann, L., & Henson, S. A. (2015). A new look at ocean carbon remineralization for estimating deepwater sequestration. *Global Biogeochemical Cycles*, *29*(7), 1044–1059. https://doi.org/10.1002/2014GB005063

Henson, S. A., Sanders, R., Madsen, E., Morris, P. J., Le Moigne, F., & Quartly, G. D. (2011). A reduced estimate of the strength of the ocean's biological carbon pump. *Geophysical Research Letters*, *38*(4). https://doi.org/10.1029/2011GL046735

Ho, T.-Y., Chou, W.-C., Wei, C.-L., Lin, F.-J., Wong, G. T. F., & Line, H.-L. (2010). Trace metal cycling in the surface water of the South China Sea: Vertical fluxes, composition, and sources. *Limnology & Oceanography*, *55*(5), 1807–1820. https://doi.org/10.4319/lo.2010.55.5.1807

Hu, J., Kawamura, H., Hong, H., & Qi, Y. (2000). A review on the currents in the South China Sea: Seasonal circulation, South China Sea Warm Current and Kuroshio intrusion. *Journal of Oceanography*, *56*(6), 607–624. https://doi.org/10.1023/A:1011117531252

Hu, J., Lan, W., Huang, B., Chiang, K.-P., & Hong, H. (2015). Low nutrient and high chlorophyll *a* coastal upwelling system – A case study in the southern Taiwan Strait. *Estuarine, Coastal and Shelf Science*, *166*, 170–177. https://doi.org/10.1016/j.ecss.2015.05.020

Huang, G., Vidal-Melgosa, S., Sichert, A., Becker, S., Fang, Y., Niggemann, J., et al. (2021). Secretion of sulfated fucans by diatoms may contribute to marine aggregate formation. *Limnology & Oceanography*, *66*(10), 3768–3782. https://doi.org/10.1002/lno.11917

Huang, Y., Fassbender, A. J., & Bushinsky, S. M. (2023). Biogenic carbon pool production maintains the Southern Ocean carbon sink. *Proceedings of the National Academy of Sciences*, *120*(18), e2217909120. https://doi.org/10.1073/pnas.2217909120

Hung, C.-C., & Gong, G.-C. (2010). POC/234Th ratios in particles collected in sediment traps in the northern South China Sea. *Estuarine, Coastal and Shelf Science*, *88*(3), 303–310. https://doi.org/10.1016/j.ecss.2010.04.008

Keil, R. (2017). Anthropogenic forcing of carbonate and organic carbon preservation in marine sediments. *Annual Review of Marine Science*, *9*(1), 151–172. https://doi.org/10.1146/annurev-marine-010816-060724

Kiko, R., Biastoch, A., Brandt, P., Cravatte, S., Hauss, H., Hummels, R., et al. (2017). Biological and physical influences on marine snowfall at the equator. *Nature Geoscience*, *10*(11), 852–858. https://doi.org/10.1038/ngeo3042

Kiko, R., Picheral, M., Antoine, D., Babin, M., Berline, L., Biard, T., et al. (2022). A global marine particle size distribution dataset obtained with the underwater vision profiler 5. *Earth System Science Data*, *14*(9), 4315–4337. https://doi.org/10.5194/essd-14-4315-2022

Kostadinov, T. S., Siegel, D. A., & Maritorena, S. (2009). Retrieval of the particle size distribution from satellite ocean color observations. *Journal of Geophysical Research*, *114*(C9). https://doi.org/10.1029/2009JC005303

Kwon, E. Y., Primeau, F., & Sarmiento, J. L. (2009). The impact of remineralization depth on the air–sea carbon balance. *Nature Geoscience*, *2*(9), 630–635. https://doi.org/10.1038/ngeo612

Li, Q., Guo, X., Zhai, W., Xu, Y., & Dai, M. (2020). Partial pressure of CO2 and air-sea CO2 fluxes in the South China Sea: Synthesis of an 18-year dataset. *Progress in Oceanography*, *182*, 102272. https://doi.org/10.1016/j.pocean.2020.102272

Li, T., Bai, Y., He, X., Xie, Y., Chen, X., Gong, F., & Pan, D. (2018). Satellite-based estimation of particulate organic carbon export in the northern South China Sea. *Journal of Geophysical Research: Oceans*, *123*(11), 8227–8246. https://doi.org/10.1029/2018JC014201

Li, W., Shang, Y., Li, C., Xu, C., Laws, E. A., Liu, X., & Huang, B. (2025). A stronger Kuroshio intrusion leads to higher chlorophyll a concentration in the northern South China Sea. *Journal of Geophysical Research: Oceans*, *130*(2), e2024JC021389. https://doi.org/10.1029/2024JC021389

Liu, H., Browning, T. J., Laws, E. A., Huang, Y., Wang, L., Shang, Y., et al. (2024). Stimulation of small phytoplankton drives enhanced sinking particle formation in a subtropical ocean eddy. *Limnology & Oceanography*, *69*(4), 834–847. https://doi.org/10.1002/lno.12529

Liu, H., Liu, X., Xiao, W., Laws, E. A., & Huang, B. (2021). Spatial and temporal variations of satellite-derived phytoplankton size classes using a three-component model bridged with temperature in Marginal Seas of the Western Pacific Ocean. *Progress in Oceanography*, *191*, 102511. https://doi.org/10.1016/j.pocean.2021.102511

Marañón, E., Van Wambeke, F., Uitz, J., Boss, E. S., Dimier, C., Dinasquet, J., et al. (2021). Deep maxima of phytoplankton biomass, primary production and bacterial production in the Mediterranean Sea. *Biogeosciences*, *18*(5), 1749–1767. https://doi.org/10.5194/bg-18-1749-2021

Mignot, A., Claustre, H., Uitz, J., Poteau, A., D'Ortenzio, F., & Xing, X. (2014). Understanding the seasonal dynamics of phytoplankton biomass and the deep chlorophyll maximum in oligotrophic environments: A bio-argo float investigation. *Global Biogeochemical Cycles*, *28*(8), 856–876. https://doi.org/10.1002/2013GB004781

Ngo, M.-H., & Hsin, Y.-C. (2021). Impacts of wind and current on the interannual variation of the summertime upwelling off southern Vietnam in the South China Sea. *Journal of Geophysical Research: Oceans*, *126*(6), e2020JC016892. https://doi.org/10.1029/2020JC016892

Nowicki, M., DeVries, T., & Siegel, D. A. (2022). Quantifying the carbon export and sequestration pathways of the ocean's biological carbon pump. *Global Biogeochemical Cycles*, *36*(3), e2021GB007083. https://doi.org/10.1029/2021GB007083

O'Connor, B. S., Muller-Karger, F. E., Nero, R. W., Hu, C., & Peebles, E. B. (2016). The role of Mississippi River discharge in offshore phytoplankton blooming in the northeastern Gulf of Mexico during August 2010. *Remote Sensing of Environment*, *173*, 133–144. https://doi.org/10.1016/j.rse.2015.11.004

Passow, U. (2002). Transparent exopolymer particles (TEP) in aquatic environments. *Progress in Oceanography*, *55*(3), 287–333. https://doi.org/10.1016/S0079-6611(02)00138-6

Picheral, M., Catalano, C., Brousseau, D., Claustre, H., Coppola, L., Leymarie, E., et al. (2022). The underwater vision profiler 6: An imaging sensor of particle size spectra and plankton, for autonomous and cabled platforms. *Limnology and Oceanography: Methods*, *20*(2), 115–129. https://doi.org/10.1002/lom3.10475

Picheral, M., Guidi, L., Stemmann, L., Karl, D. M., Iddaoud, G., & Gorsky, G. (2010). The underwater vision profiler 5: An advanced instrument for high spatial resolution studies of particle size spectra and zooplankton: Underwater vision profiler. *Limnology and Oceanography: Methods*, *8*(9), 462–473. https://doi.org/10.4319/lom.2010.8.462

Roca-Martí, M., & Puigcorbé, V. (2024). Combined use of short-lived radionuclides (^{234}Th and ^{210}Po) as tracers of sinking particles in the ocean. *Annual Review of Marine Science*, *16*(1), 551–575. https://doi.org/10.1146/annurev-marine-041923-013807

Schroeder, A., Wiesner, M. G., & Liu, Z. (2015). Fluxes of clay minerals in the South China Sea. *Earth and Planetary Science Letters*, *430*, 30–42. https://doi.org/10.1016/j.epsl.2015.08.001

Shen, J., Jiao, N., Dai, M., Wang, H., Qiu, G., Chen, J., et al. (2020). Laterally transported particles from margins serve as a major carbon and energy source for dark ocean ecosystems. *Geophysical Research Letters*, *47*(18), e2020GL088971. https://doi.org/10.1029/2020GL088971

Shih, Y.-Y., Lin, H.-H., Li, D., Hsieh, H.-H., Hung, C.-C., & Chen, C.-T. A. (2019). Elevated carbon flux in deep waters of the South China Sea. *Scientific Reports*, *9*(1), 1496. https://doi.org/10.1038/s41598-018-37726-w

Song, L., Lee, Z., Shang, S., Huang, B., Wu, J., Wu, Z., et al. (2023). On the spatial and temporal variations of primary production in the South China Sea. *IEEE Transactions on Geoscience and Remote Sensing*, *61*, 1–14. https://doi.org/10.1109/TGRS.2023.3241209

Song, Z., Kang, D., & Chai, F. (2025). Rising trends in winter phytoplankton blooms in the Northern Arabian Sea over the last two decades: Drivers and implications. *Geophysical Research Letters*, *52*(12), e2025GL116509. https://doi.org/10.1029/2025GL116509

Stukel, M. R., Décima, M., Selph, K. E., Taniguchi, D. A. A., & Landry, M. R. (2013). The role of *Synechococcus* in vertical flux in the Costa Rica upwelling dome. *Progress in Oceanography*, *112–113*, 49–59. https://doi.org/10.1016/j.pocean.2013.04.003

Tong, Z., Ma, L., Cai, S., Wang, L., Xiao, W., Huang, B., & Laws, E. A. (2023). Responses of phytoplankton communities to the effect of both river plume and coastal upwelling. *Journal of Geophysical Research: Biogeosciences*, *128*(11), e2023JG007486. https://doi.org/10.1029/2023JG007486

Tréguer, P., Bowler, C., Moriceau, B., Dutkiewicz, S., Gehlen, M., Aumont, O., et al. (2018). Influence of diatom diversity on the ocean biological carbon pump. *Nature Geoscience*, *11*(1), 27–37. https://doi.org/10.1038/s41561-017-0028-x

Trudnowska, E., Lacour, L., Ardyna, M., Rogge, A., Irisson, J. O., Waite, A. M., et al. (2021). Marine snow morphology illuminates the evolution of phytoplankton blooms and determines their subsequent vertical export. *Nature Communications*, *12*(1), 2816. https://doi.org/10.1038/s41467-021-22994-4

Tseng, C.-M., Wong, G. T. F., Lin, I.-I., Wu, C.-R., & Liu, K.-K. (2005). A unique seasonal pattern in phytoplankton biomass in low-latitude waters in the South China Sea. *Geophysical Research Letters*, *32*(8). https://doi.org/10.1029/2004GL022111

Turner, J. T. (2015). Zooplankton fecal pellets, marine snow, phytodetritus and the ocean's biological pump. *Progress in Oceanography*, *130*, 205–248. https://doi.org/10.1016/j.pocean.2014.08.005

Vidal-Melgosa, S., Sichert, A., Francis, T. B., Bartosik, D., Niggemann, J., Wichels, A., et al. (2021). Diatom fucan polysaccharide precipitates carbon during algal blooms. *Nature Communications*, *12*(1), 1150. https://doi.org/10.1038/s41467-021-21009-6

Wang, B., Huang, F., Wu, Z., Yang, J., Fu, X., & Kikuchi, K. (2009). Multi-scale climate variability of the South China Sea monsoon: A review. *Dynamics of Atmospheres and Oceans*, *47*(1), 15–37. https://doi.org/10.1016/j.dynatmoce.2008.09.004

Wei, C.-L., Lin, S.-Y., Sheu, D. D.-D., Chou, W.-C., Yi, M.-C., Santschi, P. H., & Wen, L.-S. (2011). Particle-reactive radionuclides (^{234}Th, ^{210}Pb, ^{210}Po) as tracers for the estimation of export production in the South China Sea. *Biogeosciences*, *8*(12), 3793–3808. https://doi.org/10.5194/bg-8-3793-2011

Xiao, W., Wang, L., Laws, E., Xie, Y., Chen, J., Liu, X., et al. (2018). Realized niches explain spatial gradients in seasonal abundance of phytoplankton groups in the South China Sea. *Progress in Oceanography*, *162*, 223–239. https://doi.org/10.1016/j.pocean.2018.03.008

Xie, Y., Lin, L., Xiao, W., Yu, X., Lan, W., & Huang, B. (2020). Striking seasonal pattern of primary production in the river-dominated ocean margin of the northern South China Sea (NSCS-RiOMar) revealed by new field and remotely sensed data. *Progress in Oceanography*, *189*, 102470. https://doi.org/10.1016/j.pocean.2020.102470

Xu, Z., Huang, Y., Liu, X., & Huang, B. (2025). Physical and ecological forcings drive the particle dynamics and enhanced carbon export efficiency in the tropical marginal sea [Dataset]. *Zenodo*. https://doi.org/10.5281/zenodo.16480111

Xu, Z., Zheng, Z., Xu, C., Xu, F., Chen, J., Liu, X., et al. (2025). Primary production drives varied zooplankton migration strength and twilight-zone particle dynamics across ecological gradients in the western North Pacific. *Limnology & Oceanography*, *70*(6), 1621–1635. https://doi.org/10.1002/lno.70074

Xue, H., Chai, F., Pettigrew, N., Xu, D., Shi, M., & Xu, J. (2004). Kuroshio intrusion and the circulation in the South China Sea. *Journal of Geophysical Research*, *109*(C2). https://doi.org/10.1029/2002JC001724

Yang, W., Zhao, X., Guo, L., Huang, B., Chen, M., Fang, Z., et al. (2021). Utilization of soot and 210 Po-210 Pb disequilibria to constrain particulate organic carbon fluxes in the Northeastern South China Sea. *Frontiers in Marine Science*, *8*, 694428. https://doi.org/10.3389/fmars.2021.694428

Zhou, K., Dai, M., Kao, S.-J., Wang, L., Xiu, P., Chai, F., et al. (2013). Apparent enhancement of 234Th-based particle export associated with anticyclonic eddies. *Earth and Planetary Science Letters*, *381*, 198–209. https://doi.org/10.1016/j.epsl.2013.07.039